npj | biofilms and microbiomes

Article

Published in partnership with Nanyang Technological University

https://doi.org/10.1038/s41522-025-00763-1

Periodontitis-associated *Fusobacterium nucleatum* promotes ulcerative colitis by ferroptosis-mediated gut barrier disruption

Xiaoyue Zhang[1,2], Shouzheng Cheng[1,2], Shuze Chen[1,2], Qiuhao Wang[1,2], Jeiyu Zhou[1,2], Hui Wang[1,2], Lei Cheng[1,3] ✉ & Lei Zhao[1,2] ✉

Periodontitis and ulcerative colitis (UC) are inflammatory diseases linked through the "gum-gut" axis. *Fusobacterium nucleatum*, an important periodontitis-associated pathobiont and gastrointestinal opportunist, may mediate their comorbidity. This study investigated the role of *F. nucleatum* in UC using dextran sulfate sodium-induced UC and *F. nucleatum*-induced periodontitis models. *F. nucleatum* exacerbated inflammatory alveolar bone loss and intestinal barrier dysfunction, accelerating UC severity. Integrated 16S rRNA gene sequence and LC-MS metabolomics revealed ferroptosis activation, characterized by elevated Fe^{2+} and malondialdehyde, glutathione depletion, dysregulated GPX4, FTH1, and ACSL4 expression, reduced mitochondrial membrane potential, and reactive oxygen species aggregation in the mouse colon and colonic epithelial cell CCD841. Administration of ferroptosis inhibitor Ferrostatin-1 attenuated UC by restoring intestinal permeability, preserving mucin layers, and enhancing tight junction proteins ZO-1 and CLDN-1. These findings establish *F. nucleatum* as a key mediator of periodontitis-UC comorbidity through ferroptosis-mediated gut barrier disruption, providing mechanistic insights into microbial-driven inflammatory cross-talk.

The link between periodontitis and systemic diseases has emerged as a growing field of study during the last four decades. To date, more than 50 systemic diseases have been found associated with periodontitis, including atherosclerosis[1], diabetes mellitus[2], arthritis[3], colorectal cancer (CRC)[4], and inflammatory bowel disease (IBD)[5]. Periodontitis is an immune-mediated chronic inflammatory disease that is the leading cause of tooth loss in adults and ranks as the 11th most prevalent disease worldwide[6–8]. Ulcerative colitis (UC) is a chronic, non-idiosyncratic gastrointestinal tract inflammatory and immune disorder, mainly affecting the rectum and colon, with clinical manifestations such as abdominal pain, intermittent diarrhea, and bloody, purulent stool. It is difficult to cure, has a high recurrence rate, and is closely related to the development of CRC[9,10]. Both periodontitis and UC are serious threats to human health and quality of life.

An association between UC and periodontitis was demonstrated by multiple epidemiological investigations[5,11–13]. One systematic review reported that for subtypes of IBD, periodontitis was associated with the occurrence of UC (pooled RR = 1.12, 95% CI: 1.04–1.21; $p = 0.003$; I2 = 38%), but not with Crohn's disease (pooled RR = 0.98, 95% CI: 0.92–1.04; $p = 0.475$; I2 = 0%)[13]. A retrospective cohort study based on 135,190 individuals found that after adjusting for confounders, the risk of UC in the periodontitis group was 1.5 times higher than that in the healthy control group (aHR: 1.56, 95% CI: 1.13–2.15; $p < 0.05$), suggesting that periodontitis may be an independent risk factor for UC[14]. In addition, compared with healthy people, UC patients are at higher risk of developing periodontitis[5] and often present more severe periodontal inflammation[15].

Fusobacterium nucleatum, a gram-negative anaerobic bacterium of the genus *Fusobacterium*, is a commensal member of the oral microbiota

[1]State Key Laboratory of Oral Diseases & National Center for Stomatology & National Clinical Research Center for Oral Diseases, West China Hospital of Stomatology, Sichuan University, Chengdu, 610041 Sichuan, China. [2]Department of Periodontics, West China School & Hospital of Stomatology, Sichuan University, Chengdu, China. [3]Department of Operative Dentistry and Endodontics, West China School & Hospital of Stomatology, Sichuan University, Chengdu, China. ✉e-mail: chengleidentist@163.com; Zhaolei@scu.edu.cn

primarily colonizing the deep non-attached plaque of periodontal pockets. As a core constituent of the "orange complex", it acts as a critical bridge, facilitating the adhesion and co-aggregation of early colonizers and late pathogens, thereby driving the transition of dental biofilm toward pathogenicity. Moreover, it could directly contribute to tissue destruction, immune evasion, and the maintenance of chronic inflammation[16]. Several studies reported that *F. nucleatum* oral infections alone are enough to cause periodontitis[17–19]. In addition to its involvement in the development of periodontitis, *F. nucleatum* has also been found to be associated with intestinal diseases such as CRC[20], IBD[21], and acute appendicitis (AA)[22]. *F. nucleatum* was enriched in the intestines of UC patients. Chen Y et al.[23] found that *F. nucleatum* was detected in 51.78% of intestinal tissues of UC patients and correlated with clinical course, clinical activity, and refractoriness of UC. In a dextran sodium sulfate (DSS)-induced mouse model of UC, it has been found that *F. nucleatum* promoted the development of UC by activating CARD3 through NOD2-targeted caspases and activating the IL-17 and NF-κB pathways[23]. Another study found that *F. nucleatum* could regulate macrophage polarization towards pro-inflammatory M1-type via the AKT2 pathway, thereby promoting disease progression[24]. Therefore, we postulated that *F. nucleatum* may be an important pathogenic agent for periodontitis and UC comorbidity.

Although the pathogenesis of UC is unclear, loss of intestinal barrier function is thought to be one of the key mechanisms. The intestinal epithelium is composed of a monolayer covered with mucus and serves as the body's first line of defense against external stimuli. Inappropriate intestinal epithelial cells (IECs) death could cause intestinal barrier breakdown and pathogen colonization, resulting in gastrointestinal diseases[25]. Stress, inflammation, and microbial dysbiosis cause IECs to undergo a variety of cell death pathways, including apoptosis, necrosis, necroptosis, pyroptosis, and ferroptosis[26].

Ferroptosis is a unique type of regulated cell death (RCD) proposed by Dixon in 2012, characterized by iron accumulation and lipid peroxidation[27]. Iron storage proteins include ferritin light chain and ferritin heavy chain 1 (FTH1), which can be degraded by lysosomes to increase free iron levels. Excessive iron results in lethal reactive oxygen species (ROS) via the Fenton reaction. One of the vital lipid peroxide repair systems, the glutathione/glutathione peroxidase 4 (GSH/GPX4) axis, is compromised, triggering ferroptosis[28]. Acyl-CoA synthetase long-chain family member 4 (ACSL4) is an enzyme involved in fatty acid metabolism, and up-regulation of ACSL4 increases the content of polyunsaturated fatty acids (PUFA) in phospholipids, which are susceptible to oxidative reactions and subsequent ferroptosis[29]. Furthermore, ROS oxidizes PUFA in lipid membranes, producing high lipid peroxides such as malondialdehyde (MDA) and causing membrane damage with concomitant ferroptosis[27,30]. Recent research has connected ferroptosis to UC. High dietary iron intake increases the risk of developing UC[31]. Chen Y et al.[32] found that ferroptosis occurred in DSS-induced UC mice, and ferrostatin-1 (Fer-1), a ferroptosis inhibitor, alleviated colonic inflammation through the Nrf2/HO-1 signaling pathway. Xu M et al.[33] found significant ferroptosis in IECs of UC patients and colitis mice, which was mediated by endoplasmic reticulum stress signaling, whereas in vivo application of Fer-1 was able to alleviate colitis.

In this study, we aimed to investigate the role of the periodontitis-associated *F. nucleatum* in the pathogenesis of UC and to identify possible underlying mechanisms. We observed significant inflammatory destruction of both periodontium and intestine in UC mice by *F. nucleatum* infection. The capacity of *F. nucleatum* to invade the gut barrier was demonstrated by fluorescence in situ hybridization (FISH) staining. With the help of 16S rRNA gene sequencing and LC-MS analysis of colonic content in mice, ferroptosis was found to be involved and then verified by in vivo and in vitro experiments. Inhibition of ferroptosis in mice significantly alleviated *F. nucleatum*-induced intestinal barrier dysfunction and UC progression, providing new perspectives on the pathogenesis, prevention, and therapeutic options for this comorbidity.

Results

F. nucleatum promoted periodontal and intestinal destruction in mice

The UC model was constructed through ad libitum administration of 2.5% DSS solution, while experimental periodontitis was induced via oral inoculation with *F. nucleatum* ATCC25586. Experimental groups included: healthy controls (CON), *F. nucleatum*-infected mice (FN), chronic UC mice (UC), and UC mice with concurrent *F. nucleatum* infection (UF) (Fig. 1A). Compared to gCON and gFN, the survival rates of mice in gUC and gUF declined to 90 and 70%, respectively (Fig. 1B). The weight of mice in gCON showed a continuous increase, fluctuated around the initial weight in gFN, decreased significantly in gUC, and decreased further in gUF (Fig. 1C). The disease activity index (DAI) score elevated significantly in gUC and gUF compared with gCON and gFN, and was the highest in gUF (Fig. 1D). In addition, colon length decreased progressively and statistically in four groups (Fig. 1E, F). The colon was then stained using hematoxylin and eosin (H&E) to assess its histopathological characteristics (Fig. 1G). In gCON, the colonic epithelium and crypts were intact and continuous. In gFN, the inflammatory cell infiltration was fragmented. In gUC, the crypt structure was disrupted, and there was significant infiltration of inflammatory cells in the submucosal layer, with some epithelial damage. In gUF, a large number of crypts were missing, and inflammatory cell infiltration and epithelial disruption were more pronounced. Meanwhile, H&E scores showed an increasing trend between the four groups ($p < 0.05$).

Mice exhibited periodontitis symptoms after *F. nucleatum* periodontal infection. H&E staining showed scattered inflammatory cell infiltration in gUC compared to gCON, disruption of gingival epithelial integrity, disorganization of periodontal ligament arrangement, inflammatory cell infiltration, and alveolar bone resorption in gFN. In contrast, periodontal inflammation was most significant in gUF (Fig. 1H). Micro CT showed alveolar bone resorption in gFN, characterized by an increase in the cemento-enamel junction-alveolar bone crest (CEJ-ABC) distance and trabecular separation (Td.Sp.) and a decrease in bone tissue volume (BV/TV) and bone surface area-tissue volume ratio (BS/TV) in the mandibular first molar ($p < 0.01$). Mice in gUF exhibited the highest alveolar bone resorption ($p_{CON\text{-}UF} < 0.001$). Slight alveolar bone resorption was also observed in gUC, but it was not statistically significant ($p_{CON\text{-}UC} > 0.05$) (Fig. 1I, J).

These data suggest that *F. nucleatum* is capable of destroying both periodontal and intestinal tissues, and may be a potential bridge symbiont for the association between periodontitis and UC.

F. nucleatum promoted intestinal barrier disruption in UC mice

To confirm the invasive ability of *F. nucleatum* in the intestinal tract, we performed a FISH experiment (Fig. 2A). The results showed that *F. nucleatum* from periodontal infections accumulated in the intestinal lumen and adhered to the IECs. In gFN, the number of invaded *F. nucleatum* in the lamina propria was limited ($p_{CON\text{-}FN} > 0.05$). In contrast, a large amount of *F. nucleatum* could be seen invading the deeper layers in gUF ($p_{CON\text{-}UF} < 0.001$). This suggests that the intestinal barrier is effective in isolating pathogenic *F. nucleatum* invasion in physiological states. Furthermore, *F. nucleatum* abundance was significantly higher in gUC intestinal tissue ($p_{CON\text{-}UC} < 0.001$). We also confirmed that elevated *F. nucleatum* levels in the colon of the gUF were oral in origin (Supplementary Fig. 1 and Supplementary Table 3).

Next, we tested the intestinal barrier function. Alcian blue/periodic acid-Schiff (AB-PAS) staining results showed that *F. nucleatum* aggravated intestinal mucus layer destruction in UC ($p_{UC\text{-}UF} < 0.05$) (Fig. 2B). Transmission electron microscopy (TEM) revealed that the tight junctions (TJs) between the IECs were intact, and the intestinal villi were neatly arranged and moderately dense in gCON. Although the TJs appeared intact, there were fewer intestinal villi in gFN. In gUC, typical disruption of TJs and loss of villi were observed. While in gUF, the intestinal villi were largely absent, TJs were disrupted, the intercellular gap widened, and the organelles were detached (Fig. 2C). Serum FD4

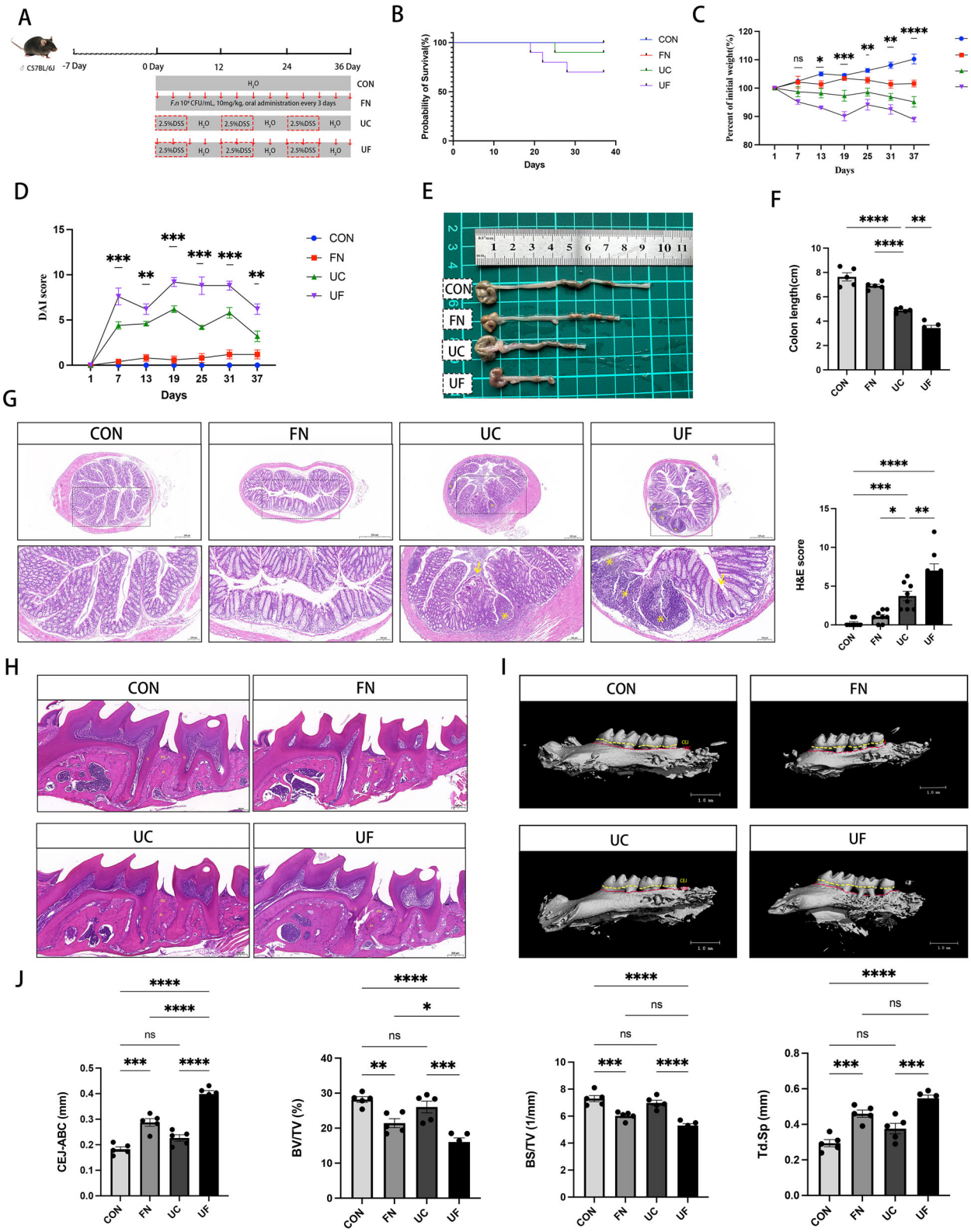

Fig. 1 | *F.nucleatum* promoted periodontal and intestinal destruction in mice. **A** Schematic representation and study design. **B** The survival rate of mice (% of initial) ($n = 10$). **C** Weight change of mice (% of initial) ($n = 10$). **D** Disease activity index (DAI) scores of mice ($n = 10$). **E** Representative images of the colon and **F** quantification of colon length (scale: 1 cm) ($n = 5$). **G** Histological images of the colon (scale: 50 μm) (left) and the H&E score (right). Yellow "*" indicates inflammatory cell infiltration, and yellow arrows indicate epithelial disruption ($n = 8$). **H** Histological images of the periodontium (scale: 200 μm). AL alveolar bone, PDL periodontal ligament, D dentin, black arrows: stripped junction epithelium ($n = 5$). **I** Representative Micro CT images (scale: 10 μm), Yellow line: ABC, red line: CEJ ($n = 5$). **J** The analysis of the distance from the cement-to-enamel junction-alveolar bone crest, CEJ-ABC (mm), the value of bone volume/tissue volume, BV/TV (%), bone surface area-tissue volume ratio, (BS/TV) (1/mm) and the trabecular separation, Td.Sp (mm). All data represent the mean ± SEM. Each dot indicated an individual mouse. *$P < 0.05$, **$p < 0.01$, ***$P < 0.001$, ****$p < 0.0001$, by one-way or two-way ANOVA, followed by a post hoc test.

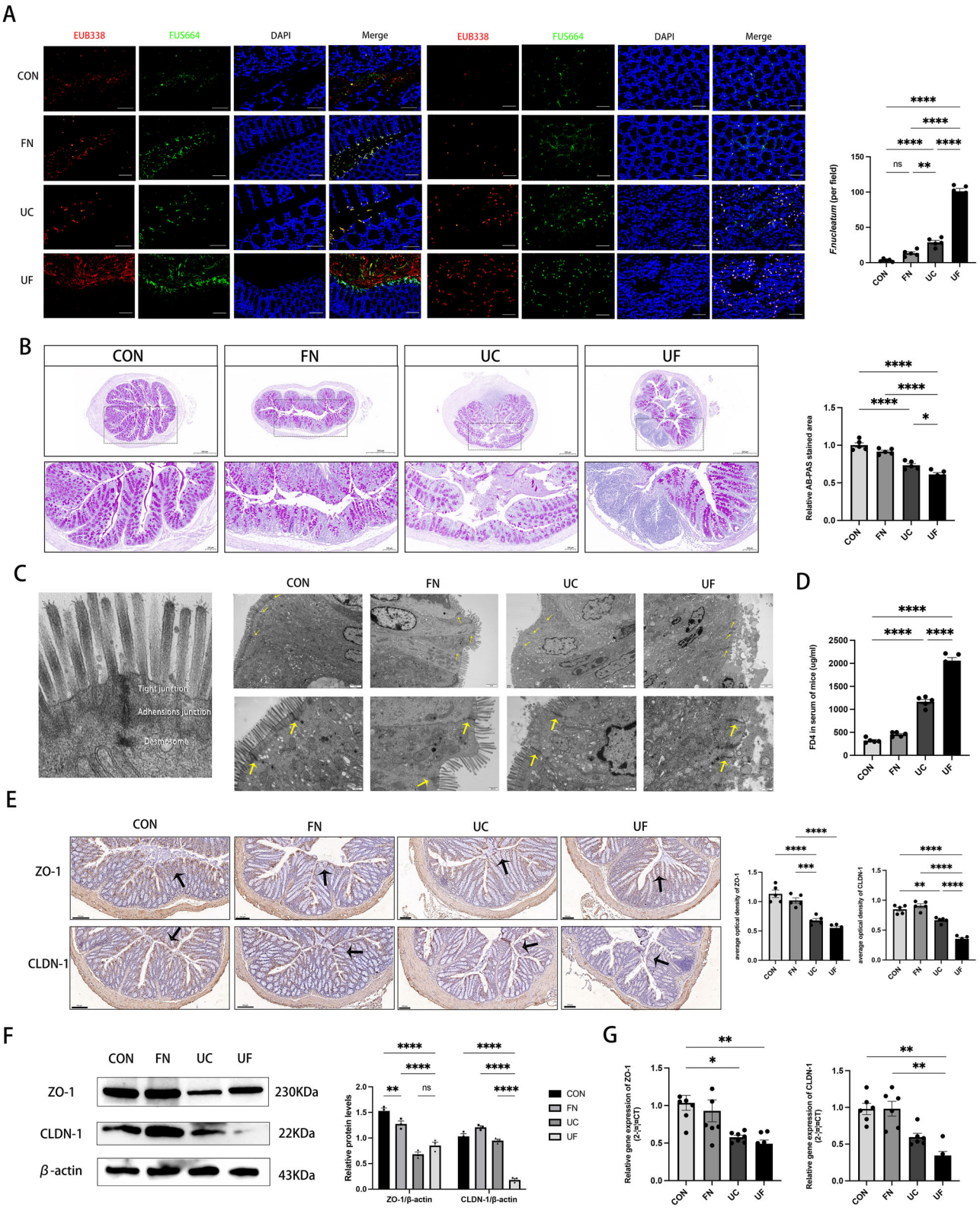

concentration, representing intestinal permeability, increased substantially following *F. nucleatum* challenges ($p_{UC\text{-}UF} < 0.0001$) (Fig. 2D). We then detected the expression of the TJs proteins Zona occludens 1 (ZO-1) and Claudin 1 (CLDN-1) using immunohistochemical (IHC) staining and western blot (WB). In comparison to gCON, ZO-1 and CLDN-1 protein expressions were lower in gUC and gUF (Fig. 2E, F), as well as mRNA ($p < 0.05$) (Fig. 2G).

These results showed that *F. nucleatum* could aggravate the intestinal barrier disruption in UC mice.

F. nucleatum promoted UC development associated with ferroptosis

The colonic content of the mice was analyzed using 16S rRNA gene sequencing and the LC-MS technique. The rarefaction curves flattened, and

Fig. 2 | *F.nucleatum* promoted intestinal barrier disruption in UC mice. **A** Representative fluorescence in situ hybridization (FISH) image assessing the amount of *F.nucleatum* in the intestinal lumen and intestinal tissue of mice (left) and the quantification in panel (right). EUB338 (red) is a Cy3-conjugated universal bacterial oligonucleotide probe, FUS664 (green) is a FAM-conjugated *F. nucleatum*-specific oligonucleotide probe (scale: 50 μm) ($n = 5$). **B** Alcian blue/periodic acid-Schiff (AB-PAS) staining of the colon (left) and the relative quantification of the stained area (right) (scale: 500 μm, up; 100 μm, down) ($n = 5$). **C** Transmission electron microscopy (TEM) of the physiologic structure of the epithelial junction complex of the mouse colon (left). TEM of mice intestinal epithelium, with yellow arrowheads indicating the junction complex (scale: 2 μm, up; 500 nm, down) (right) ($n = 5$). **D** FITC-dextran (FD4) permeability assay evaluated mice intestinal epithelial permeability ($n = 5$). **E** Immunohistochemical staining for ZO-1 and CLDN-1 of mice colon (scale: 100 μm) and the average optical density was shown on the right side. **F** Western blotting analysis of ZO-1 and CLDN-1 of mice colon and quantification. β-actin was used as the loading control ($n = 3$). **G** RT-qPCR measured the relative mRNA levels of ZO-1 and CLDN-1 in the colon of mice. All data represent the mean ± SEM. Each dot indicated an individual mouse. $^{*}P < 0.05$, $^{**}p < 0.01$, $^{***}P < 0.001$, $^{****}p < 0.0001$, by one-way or two-way ANOVA, followed by a post hoc test.

the sequencing data reached saturation, enabling coverage of most of the species. Gut microbial diversity was significantly reduced in gUF (Supplementary Fig. 2). Comparative analysis of Beta diversity showed a clear trend of dispersion between gCON and gUF, suggesting significant differences in community microbes (Fig. 3A). At the phylum level, the community abundance composition exhibited a decline in *Firmicutes* and *Verrucomicrobiota*, while *Proteobacteria* and *Bacteroidota* showed an increase (Fig. 3B). Analysis of the species with significant differences based on LEfSe revealed that *Fusobacteriaceae* was one of the dominant bacteria in the gFN, gUC, and gUF (Fig. 3C). The sample-species relationships are shown in Supplementary Fig. 3. Further functional abundance changes of the microbial community were predicted by PICRUSt2, and the heatmap showed that "cell growth and death" from "cellular process" was implicated in the differential pathways between the four groups, with "necroptosis, ferroptosis, and apoptosis" as the specific mechanisms (Fig. 3D and Supplementary Tables 4–6).

Based on the metabolomic analysis, the PCA score plot revealed differences between gCON and gUC (Fig. 3E). The Venn diagram showed the different metabolite compositions between groups (Fig. 3F). Diagram after comparing and statistically mapping intestinal metabolites with categorization information from the HMDB 4.0 database was shown in Fig. 3G. The KEGG functional pathway identified "ferroptosis" and "apoptosis" as the main pathways involved in "cell growth and death" (Fig. 2H and Supplementary Table 7). KEGG pathway enrichment and iPath metabolic pathway analyses are shown in Supplementary Figs. 4, 5.

The combined 16S rRNA gene sequencing and LC-MS results suggested that the aggravation of UC by *F. nucleatum* infection may be associated with ferroptosis.

F. nucleatum induced ferroptosis in the colon of UC mice

To confirm this hypothesis, we examined the expression of the ferroptosis regulators GPX4, FTH1, and ACSL4. IHC staining and WB of mouse colon showed decreased GPX4 protein levels but increased FTH1 and ACSL4 protein levels (Fig. 4A-C). RT-qPCR identified changes in the mRNA levels of GPX4, FTH1, and ACSL4, which were consistent with the protein results (Fig. 4D). Moreover, MDA and iron contents, particularly ferroptosis-related Fe^{2+}, were upregulated in the colon, whereas the reduction ratio of GSH was downregulated (Fig. 4E-G). These results suggested that *F. nucleatum* infection increased susceptibility to ferroptosis and exacerbated colonic ferroptosis in UC mice.

IHC staining revealed that cells with altered expression of ferroptosis regulators were localized predominantly within the epithelium. We therefore performed double immunofluorescence staining for the epithelial cell marker CK18 and ferroptosis marker GPX4. The results revealed that the overlapping signals of CK18 and GPX4 were significantly reduced in gUC and gUF compared with gCON and gFN (Fig. 4H). Based on the above data, we hypothesized that *F. nucleatum* adheres to and induces ferroptosis in IECs, thereby disrupting the gut barrier.

F. nucleatum induced ferroptosis in the colonic epithelial cells

To further clarify the effect of *F. nucleatum* on the IECs, we investigated ferroptosis in the normal colonic epithelial cell CCD-841 (ATCC CRL-1790). DSS solutions and *F. nucleatum* suspensions were selected at appropriate concentrations and co-cultured with the cells for 24 h (Supplementary Fig. 6). Cell viability and LDH release were then assessed. *F. nucleatum* significantly inhibited cell proliferation and caused cell damage (Fig. 5A, B). Furthermore, *F. nucleatum* promoted cell ferroptosis, as evidenced by increased MDA levels, decreased GSH ratios, and intercellular Fe^{2+} aggregation (Fig. 5C, D, G). RT-qPCR and WB results showed decreased GPX4 and increased FTH1 and ACSL4 mRNA and protein levels, consistent with in vivo experiments. (Fig. 5E, F). The IHC staining results further confirmed the trend changes in GPX4, FTH1, and ACSL4 (Fig. 5H).

Next, we introduced the ferroptosis inhibitors Fer-1 and deferoxamine (DFO), determined their optimal concentrations (data not shown), and found that Fer-1 outperformed DFO in rescuing CCD-841 cell activity (Supplementary Fig. 7). Fer-1 significantly inhibited *F. nucleatum*-induced intercellular ROS aggregation and mitochondrial membrane potential (MMP) decrease, which are characteristic of ferroptosis (Fig. 5I, J).

These studies suggested that *F.nucleatum* increased cell ferroptosis in IECs and that Fer-1 could partially rescue this process.

Ferroptosis inhibitor rescued *F.nucleatum*-induced intestinal barrier disruption in UC mice

To validate the effect of inhibiting ferroptosis on the progression of UC with *F.nucleatum* infection, we added Fer-1 treatment to the original grouping, and the mice were modeled as shown in Fig. 6A. The safety of Fer-1 intraperitoneal injection has been tested (Supplementary Fig. 8). Compared to gUC and gUF, the survival rates of mice in gUC+Fer-1 and gUF + Fer-1 increased from 85.7 to 100% and from 62.5 to 85.7%, respectively (Fig. 6B). From day 25 of modeling, the weight of mice in gUC+Fer-1 and gUF+Fer-1 were significantly higher than those in gUC and gUF ($p < 0.05$) (Fig. 6C). The DAI score was significantly decreased in gUF + Fer-1 compared to gUF and even lower than that of gUC + Fer-1 after 31 days of modeling ($p < 0.001$) (Fig. 6D). Colon length was significantly increased in gUC + Fer-1 and gUF + Fer-1 compared to gUC and gUF ($p < 0.01$). In addition, there was no statistically significant difference between gUC+Fer-1 and gUF+Fer-1 (Fig. 6E, F). These results suggested that inhibition of ferroptosis is effective in suppressing disease progression in UC with *F.nucleatum* infection.

Next, we measured the intestinal barrier following the inhibition of ferroptosis. Serum FD4 concentration was significantly lower in gUF + Fer-1 compared with gUF ($p < 0.0001$) but was not statistically different in gUC and gUC+Fer-1 (Fig. 6G). The histopathological changes were evaluated using H&E staining and AB-PAS staining, as shown in Fig. 6H, I. Compared to gUC and gUF, lighter epithelial damage, fewer inflammatory cell infiltration, and less crypt disruption as well as increased mucus production were observed in gUC + Fer-1 and gUF + Fer-1. WB and IHC staining showed that ZO-1 and CLDN-1 protein expressions were significantly upregulated in gUC + Fer-1 and gUF+Fer-1 compared with gUC and gUF ($p < 0.05$) (Fig. 6J, K). These results proved that the application of ferroptosis inhibitors can significantly rescue intestinal barrier disruption aggravated by *F. nucleatum*.

Discussion

F. nucleatum is a resident bacterium in the oropharynx and gastrointestinal tract of humans. It has a wide range of virulence factors, including

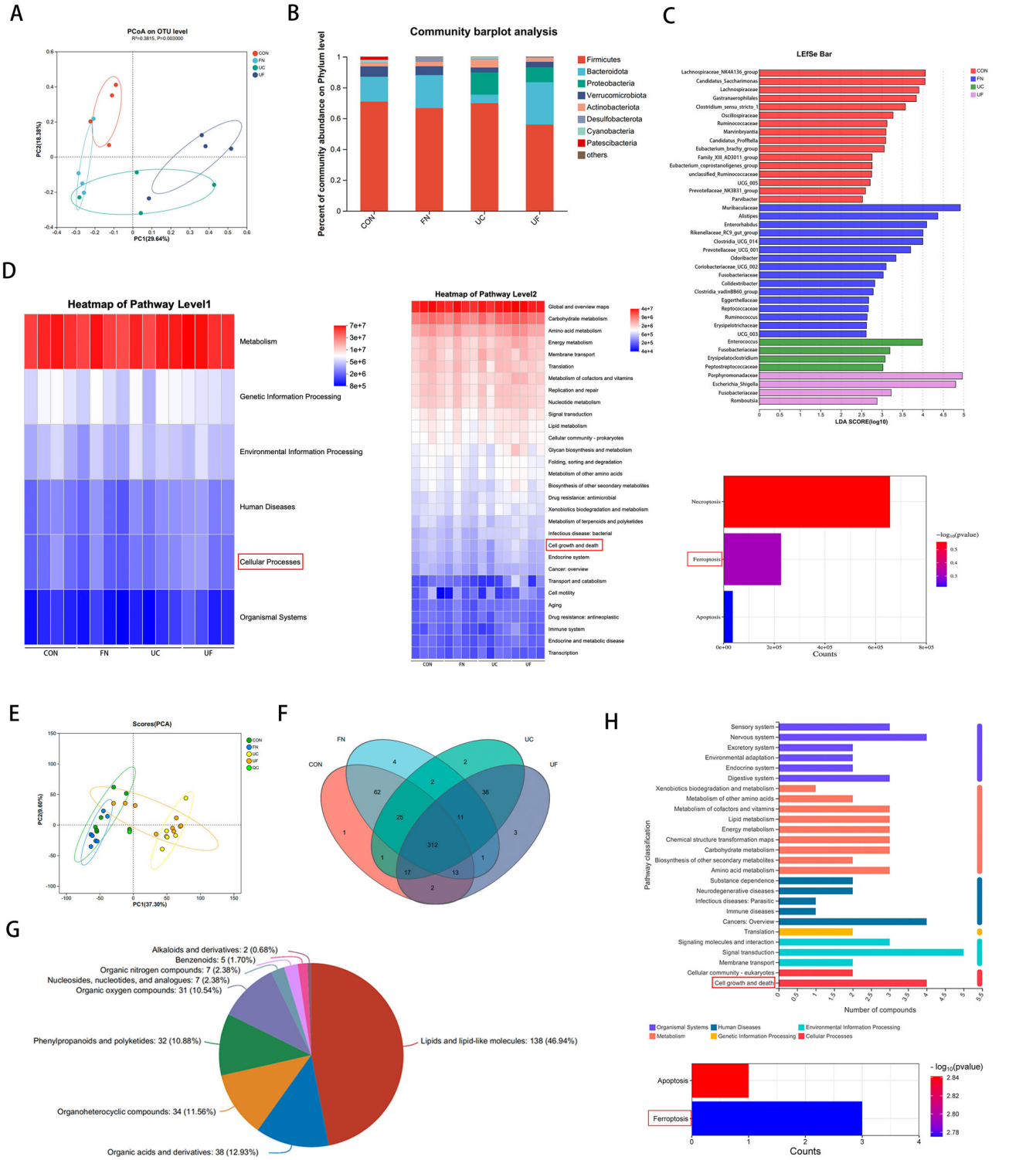

Fig. 3 | *F.nucleatum* promoted UC development associated with ferroptosis. **A** Principal coordinate analysis (PCoA) was performed on unweighted uniFrac distances to analyze differences in microbial community structure. **B** Community barplot analysis on phylum level. **C** The most differentially abundant taxa of characteristic microorganisms by LEfSe (LDA >2). LDA Score: linear discriminant analysis score. **D** PICRRUSt2 functional prediction heatmap (KEGG functional abundance statistics). The horizontal coordinate is the group name, the vertical coordinate is the pathway level 1/2/3 functional name, and the color gradient of the color block shows the change of different functional abundance in the group. **E** Principal component analysis (PCA): Samples (including QC samples) were subjected to principal component analysis, which provided a preliminary understanding of the overall metabolic differences between the four groups and the magnitude of variability between samples within groups. **F** Venn Diagram: Understand the metabolite composition of different groups, different colors represent different subgroups, overlapping numbers represent the number of metabolites common to multiple subgroups, and non-overlapping numbers represent the number of metabolites specific to the corresponding subgroups. **G** Comparison of the HMDB 4.0 database to obtain taxonomic information and statistical mapping of metabolites. **H** Metabolomic analysis of intestinal contents in mice. The vertical coordinate is the secondary classification of the KEGG metabolic pathway, and the horizontal coordinate is the number of compounds annotated to the pathway.

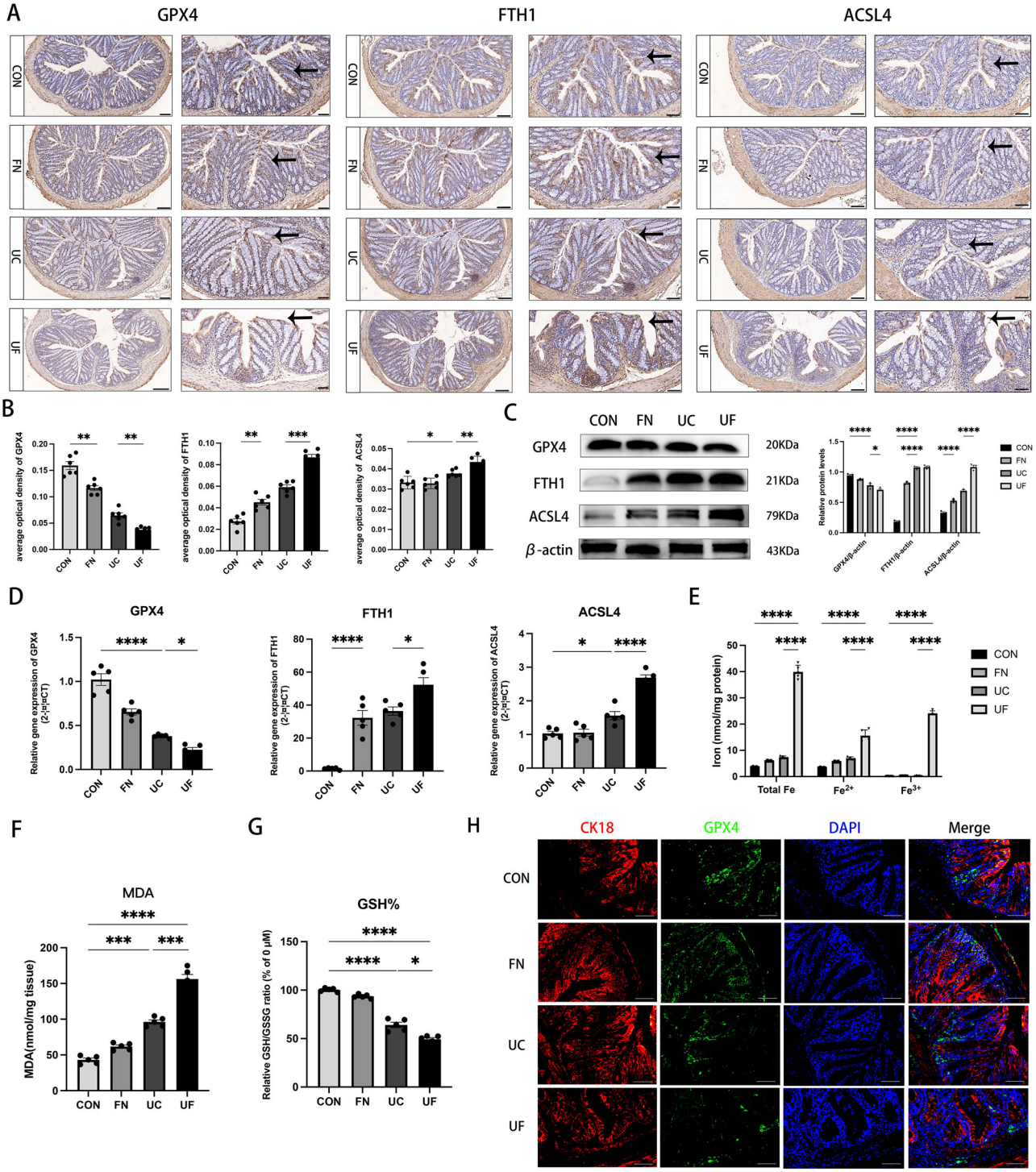

Fig. 4 | *F.nucleatum* induced ferroptosis in the colon of UC mice.
A Immunohistochemical staining for GPX4, FTH1, and ACSL4 (scale: 100 μm, left; 50 μm, right). Black arrows indicated expression-positive cells. **B** The average optical density of GPX4, FTH1, and ACSL4 was shown on the right side ($n = 6$). **C** Western blotting analysis of GPX4, FTH1, and ACSL4 and quantification. β-actin was used as the loading control ($n = 3$). **D** RT-qPCR measured the relative mRNA levels of GPX4, FTH1, and ACSL4 ($n = 5$). **E** Iron Assay Kit determined the iron levels ($n = 5$). **F** MDA Assay Kit measured the MDA levels ($n = 5$). **G** GSH and GSSG Assay Kit measured the relative GSH/ GSSG ratio (GSH%) ($n = 5$). **H** Double immunofluorescent staining for GPX4 and cytokeratin 18 (CK18) (scale: 50 μm) ($n = 3$). Each dot indicated an individual mouse. All data represent the mean ± SEM. $^{*}P < 0.05$, $^{**}p < 0.01$, $^{***}P < 0.001$, $^{****}p < 0.0001$, by one-way or two-way ANOVA, followed by a post hoc test.

lipopolysaccharide, FadA, Fap2, FadD, FomA, FplA, and Fad-I that allow it to survive and thrive in an inflammatory environment[34,35]. Dzink J et al.[36] divided *F. nucleatum* into three subspecies: (1) *Fusobacterium nucleatum subsp. nucleatum*, ATCC25586; (2) *Fusobacterium nucleatum subsp. polymorphum*, ATCC10953; and (3) *Fusobacterium nucleatum subsp. vincentii*, ATCC49256. Of all the subtypes, *F. nucleatum* ATCC25586 was isolated mainly from periodontitis sites and was most frequently detected in subgingival plaque biofilms[37]. In addition, *F. nucleatum* ATCC25586 is one of the standard strains of common gastrointestinal bacteria and is highly associated with intestinal inflammation and CRC[38,39]. Therefore, in this

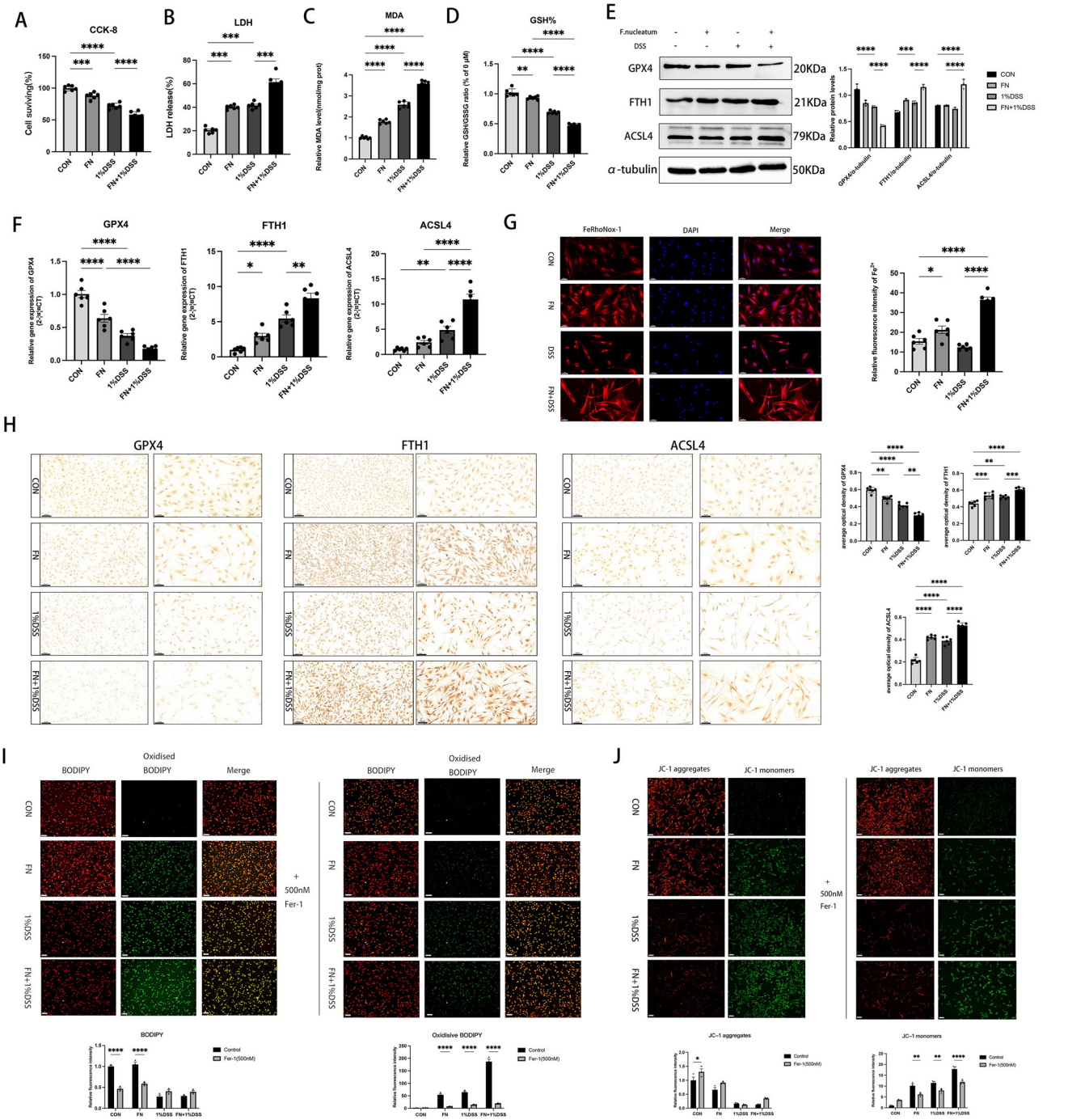

Fig. 5 | *F. nucleatum* induced ferroptosis in the colonic epithelial cells. A CCK-8 Assay Kit determined the cell survival (%) of CCD-841($n = 6$). **B** LDH Assay Kit determined the LDH releasing (%) of CCD-841($n = 6$). **C** MDA Assay Kit measured the MDA levels of CCD-841($n = 6$). **D** GSH and GSSG Assay Kit measured the relative GSH/ GSSG ratio (GSH%) of CCD-841($n = 6$). **E** Western blotting analysis of GPX4, FTH1, and ACSL4 and quantification. α-tubulin was used as the loading control ($n = 3$). **F** RT-qPCR measured the relative mRNA level of GPX4, FTH1, and ACSL4 ($n = 6$). **G** FeRhoNox-1 fluorescence staining for detecting Fe^{2+} of CCD-841 and quantification were shown on the right ($n = 6$). **H** Immunohistochemical staining for GPX4, FTH1, and ACSL4 (scale: 200 μm, left; 100 μm, right). The average optical density of GPX4, FTH1, and ACSL4 were shown on the right ($n = 6$). After the introduction of Fer-1 and DFO, **I** C11-BODIPY staining assessed the ROS level of CCD-841 and quantification ($n = 3$). Oxidation state BODIPY signal (green), reduction state signal (red). **J** JC-1 fluorescence staining detected the mitochondrial membrane potential (MMP) of CCD-841 and quantification. When MMP is high, JC-1 aggregates in the matrix of mitochondria and produces red fluorescence; at lower MMP, green fluorescence is produced ($n = 3$). Each dot indicated an individual mouse. All data represent the mean ± SEM. $^{*}P < 0.05$, $^{**}p < 0.01$, $^{***}P < 0.001$, $^{****}p < 0.0001$, by one-way or two-way ANOVA, followed by a post hoc test.

experiment, *F. nucleatum* ATCC25586 was selected as a representative subspecies of periodontal pathogenic bacteria infecting mice to investigate its role in UC progression.

The human gastrointestinal tract and oral cavity are the first and second largest bacterial repositories, harboring more than 500 and 770 species, respectively[40]. These bacteria coexist with the host immune system in a

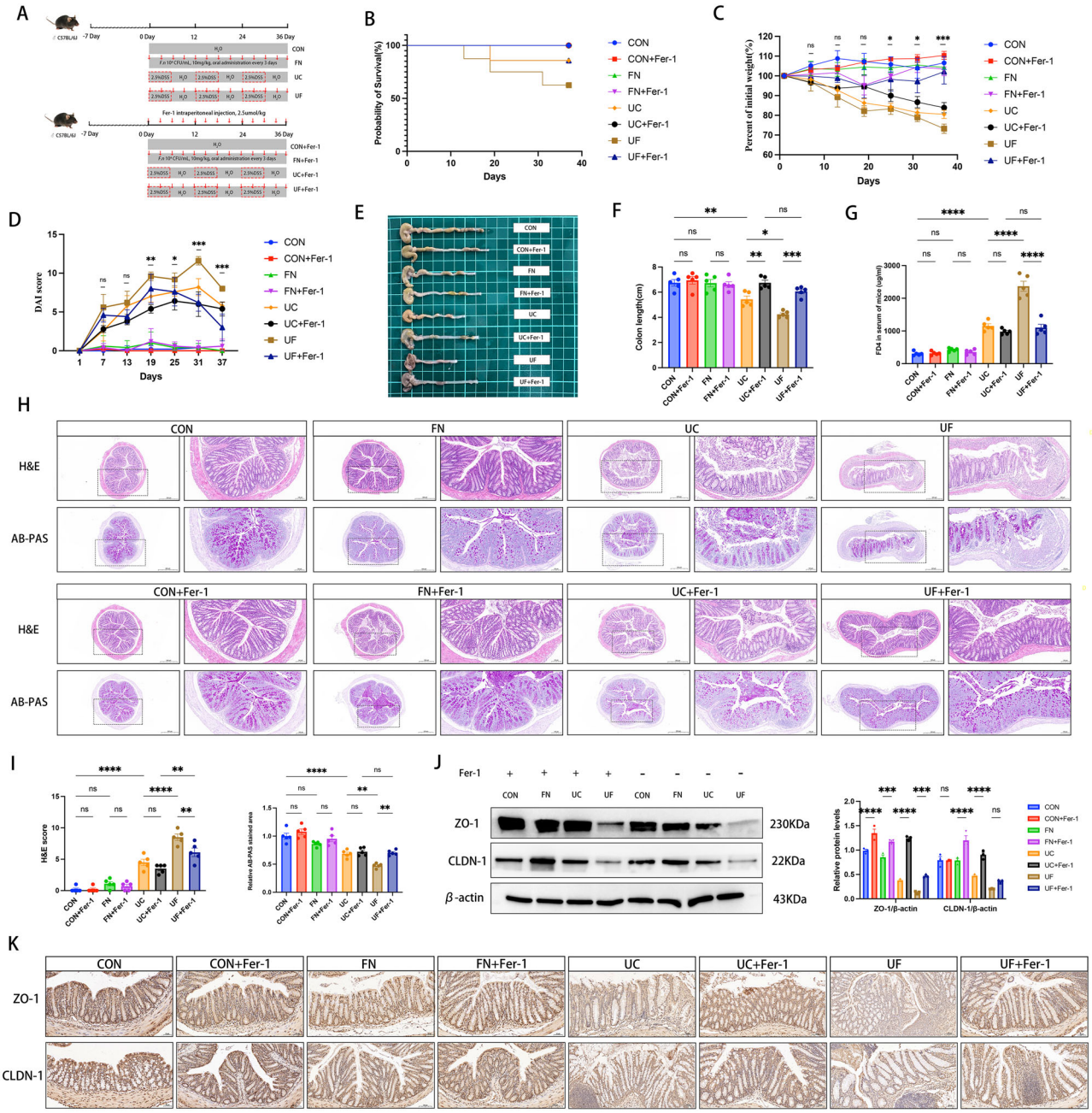

Fig. 6 | Ferroptosis inhibitor rescued *F. nucleatum*-induced intestinal barrier disruption in UC mice. A Schematic representation and study design. **B** The survival rate of mice (% of initial) ($n = 10$). **C** Weight change of mice (% of initial) ($n = 10$). **D** DAI scores of mice ($n = 10$). **E** Representative images of the colon and **F** quantification of colon length (scale: 1 cm) ($n = 5$). **G** FD4 permeability assay evaluated mice intestinal epithelial permeability ($n = 5$). **H** Histological images and AB-PAS staining of the colon (scale: 500 μm, left; scale: 100 μm, right) ($n = 5$). **I** H&E score (left) and the relative quantification of the stained area (right) ($n = 5$). **J** Western blotting analysis of ZO-1 and CLDN-1 of mice colon and quantification. β-actin was used as the loading control ($n = 3$). **K** Immunohistochemical staining for ZO-1 and CLDN-1 of mice colon (scale: 50, 100 μm) and the average optical density was shown on the right side. Each dot indicated an individual mouse. All data represent the mean ± SEM. $^{*}P < 0.05$, $^{**}p < 0.01$, $^{***}P < 0.001$, $^{****}p < 0.0001$, by one-way or two-way ANOVA, followed by a post hoc test.

dynamic equilibrium, maintaining niche homeostasis. Recent research has linked gastrointestinal inflammation to periodontal bacteria, including *Fusobacterium nucleatum, Fusobacterium varium, Porphyromonas gingivalis, Atopobium parvulum, Campylobacter concisus, Staphylococcus aureus, Klebsiella spp., and Enterobacter spp.*[41,42]. With the booming development of high-throughput sequencing technology and the continuous improvement of microbial and metabolite databases, the roles of intestinal flora and their metabolites in intestinal diseases have been continuously revealed. By 16S rRNA gene sequencing technology, the similarity between subgingival biofilm composition and intestinal flora changes in UC patients was found, and abnormal enrichment of periodontal pathogens could be detected in the intestine[41,43,44]. The gut microbiota in UC patients shows higher similarity to oral microbiota compared to healthy controls, suggesting that oral-gut microbial translocation could potentially drive periodontitis-associated UC pathogenesis[45,46]. Thus, periodontal and intestinal symbiont–host interactions may be a potential common etiology of immunoinflammatory diseases in both sites.

Periodontal-derived bacteria can migrate to the gastrointestinal tract via the saliva or hematopoietic routes[44]. Kitamoto S et al.[47,48] suggested that at least two conditions must be met for ectopic colonization of the

gut by oral pathogens. First, the colonization resistance of the resident microbiota in the gut is disrupted, and second, inflammation in the oral cavity causes the number of oral pathogens to reach a certain threshold in the gut. Our previous study showed that oral gavage of *F. nucleatum* caused intestinal inflammation and microbiota dysbiosis in UC mice, which were highly associated with a decrease in probiotics such as *Bifidobacterium* and *Faecalibacterium*, as well as an increase in opportunistic pathogen *Escherichia-Shigella*[18]. In this study, through 16S rRNA gene sequencing and metabolomics analysis of mouse colonic contents, we found that periodontal infection with *F.nucleatum* also exacerbated gut microbiota dysbiosis and metabolic disturbances. FUS664 (green) is a FITC-conjugated *F.nucleatum*-specific oligonucleotide probe. FISH staining results showed that green signals were mainly localized in the intestinal lumen in gCON and gFN, being separated by the epithelial layer, with limited green signals detected in the lamina propria. In contrast, a large number of green signals were observed in the lamina propria of gUC and gUF. The absolute quantitative qPCR analysis of *F.nucleatum* ATCC25586 in colon tissues revealed its highest enrichment in the UF group(Supplementary Fig. 1), further confirming this observation. However, our data showed that the LDA scores of *Fusobacteriaceae* were similar between gUC and gUF. This may be due to the technical limitations of 16S gene sequencing targeting the V3–V4 regions, including limited taxonomic resolution and the potential for misclassification of closely related taxonomic units. To address these challenges, more precise microbial sequencing approaches such as metatranscriptomics and the BarBIQ method (Barcoded Bacterial Identification and Quantification)[49] were needed in future studies.

Our findings revealed that *F. nucleatum* exhibited limited colonic colonization under physiological conditions but demonstrated extensive ectopic proliferation in UC mice, with this dysbiotic expansion being directly correlated with the disruption of the intestinal barrier. Histopathological staining of the colon with H&E and AB-PAS indicated intestinal inflammation and destruction of the mucus layer. TEM revealed the disruption of epithelial junctions. IHC, WB, and RT-qPCR analyses showed decreased expression of tight junction proteins (ZO-1 and CLDN-1). Collectively, these results confirmed *F. nucleatum*-mediated disruption of the intestinal barrier in UC mice, consistent with prior studies[18,23,24].

KEGG enrichment analysis further suggested ferroptosis as a potential mechanistic factor, a perspective validated through both in vivo and in vitro experiments. *F. nucleatum* was shown to induce ferroptosis in intestinal epithelial cells, characterized by elevated Fe^{2+} and MDA levels, depletion of GSH/GPX4, upregulated expression of FTH1 and ACSL4, along with reduced MMP and ROS accumulation. Notably, the ferroptosis inhibitor Fer-1 not only significantly mitigated cellular damage and ferroptosis in vitro but also demonstrated safety and therapeutic efficacy in vivo, rescuing barrier dysfunction in *F. nucleatum*-infected UC mice. Previous studies have demonstrated that lipopolysaccharide from *F. nucleatum* induces autophagy in IECs to promote UC[50], while *F. nucleatum*-derived extracellular vesicles disrupt the intestinal barrier via RIPK1-mediated IEC death[51]. Our study is the first to reveal that the *F. nucleatum* triggers IEC ferroptosis.

Furthermore, mild alveolar bone resorption and inflammation were observed in gUC mice, while the gUF exhibited more severe inflammatory bone loss compared to the gUC, suggesting that UC may exert a potential impact on periodontitis. Recent studies have shown that DSS-induced colitis might exacerbate periodontitis through the NOX2/ROS axis-mediated polarization of M1-type macrophages[52]. However, research in this area remains limited, warranting further investigation.

In conclusion, our findings support the substantial link between periodontitis and UC from the perspective of the symbiont *F. nucleatum*. *F. nucleatum* exacerbated UC by promoting IECs ferroptosis-mediated intestinal barrier dysfunction. This study shed light on host-symbiont interactions and highlighted that ferroptosis inhibition may be a promising therapeutic approach to their comorbidity.

Methods

Bacterial culture

State Key Laboratory of Oral Diseases & National Center for Stomatology provided *F. nucleatum* (ATCC25586). *F. nucleatum* was inoculated in blood agar plates anaerobically at 37 °C for 2 days, and a single colony was transferred to brain heart infusion broth with Vitamin K (0.2 μg mL^{-1}) and heme chloride (5 μg mL^{-1}). Regularly check for bacterial contamination under an oil microscope.

Animals and study design

Animal welfare and experimental protocols followed the ARRIVE guidelines (Animal Research: Reporting of In Vivo Experiments). Specific-pathogen-free (SPF) C57BL/6J mice (male, 6–8 weeks, 20–22 g) were housed in the SPF facility (environmental temperature remained around 23 °C and humidity around 55%). After 7–14 days of acclimation, mice were randomly divided into four groups ($n = 10$, each group): healthy control (CON), *F. nucleatum* infection (FN), chronic UC (UC), and UC with *F. nucleatum* infection (UF). The chronic UC model was established by freely drinking 2.5% DSS (molecular weight 36–50 kDa, MP Biomedicals, Inc., USA) solution for 6 days, followed by distilled water for 6 days, and the model was repeated for three cycles, 36 days in total. *F. nucleatum* was centrifuged at 4000 rpm for 10 min at 4 °C, diluted with PBS to a concentration of 1×10^9 CFU mL^{-1}. A suspension of *F. nucleatum* was inoculated around the periodontium of the maxillary molar every 3 days at a dose of 10 ml kg^{-1}. Later, mice were randomly divided into eight groups: CON ($n = 5$), CON+Fer-1 ($n = 5$), FN ($n = 5$), FN + Fer-1 ($n = 5$), UC ($n = 8$), UC + Fer-1 ($n = 8$), UF ($n = 8$), UF + Fer-1 ($n = 8$). On the basis of the previous four-group modeling approach, intraperitoneal injections of ferrostatin-1 (2.5 μmol kg^{-1}) every 3 days. The survival rate, weight, and DAI score of mice were monitored (Supplementary Table 1). Mice were anesthetized via inhalation of 3% isoflurane (vol/vol in oxygen) using a calibrated vaporizer, with anesthesia depth confirmed by absence of pedal withdrawal reflex. Euthanasia was performed via cervical dislocation under deep anesthesia (5% isoflurane for ≥2 min). Following euthanasia, blood, colon tissue, colonic contents, and maxillae were collected.

Ethics statement. This study was approved by the Ethics Committee of West China School of Stomatology, Sichuan University (Approval ID WCHSIRB-D- 2021-007).

Cell culture and models

Human normal colon epithelial cells CCD-841 (ATCC CRL-1790) were purchased from ATCC (Manassas, VA, USA). CCD-841 cells were cultured in Dulbecco's modified Eagle's medium supplemented with 10% fetal bovine serum (Gibco, NY, USA) and 1% P/S in a humidified atmosphere containing 5% CO2 at 37 °C. Cells were seeded into six-well plates at a density of 2×10^5 cells/well. Cells were serum-starved for 2 h prior to *F. nucleatum* coculture to eliminate FBS interference. Subsequently, cells were treated with DSS at various concentrations or co-cultured with *F. nucleatum* resuspended in cell medium (Multiplicity of infection:100:1) without FBS for 24 h to establish the injury model.

Cell viability assay and cell injury detection

Cell viability was assessed by Cell Counting Kit-8 (CCK-8) Assay (B5058, APExBIO, USA). Cell injury was measured by releasing lactate dehydrogenase (LDH) with the LDH Cytotoxicity Assay Kit (C0016, Beyotime, China).

Iron, MDA, and GSH determination

The iron concentration of mice colon tissue was assessed with an Iron Assay Kit (ab83366, Abcam, UK). The determination of MDA and GSH were determined by Lipid Peroxidation MDA Assay Kit (S0131M, Beyotime, China) and GSH and GSSG Assay Kit (S0053, Beyotime, China), respectively.

Western blot analysis

The total proteins of colon tissue and cells were obtained by Total Protein Extraction Kit (PE001, Signalway Antibody/SAB, USA), and the protein concentrations were assessed by BCA Protein Assay Kit (P0010, Beyotime, China). The lysates were separated by SDS-PAGE and transferred to polyvinylidene difluoride membranes (IPVH 00010, Millipore, USA). Primary antibodies of GPX4, FTH1, ACSL4, ZO-1, and CLDN-1 (Host species: Rabbit monoclonal) were diluted 1:1000. β-actin and α-tubulin (Host species: Rabbit monoclonal) were diluted 1:5000. The secondary antibodies (Goat anti-rabbit IgG-HRP) were diluted 1:10,000 (HUABIO, China). Membranes were developed using SuperKine West Femto Maximum Sensitivity Substrate (BMU102-CN, Abbkine Scientific, China). The protein signals were detected by the ChemiDocTMXRS+ system (Bio-Rad, USA). β-actin and α-tubulin were used as the internal control.

Quantitative real-time polymerase chain reaction (qRT-PCR)

The total RNA of the mice colon was extracted by an RNA extraction kit (RP55012, Bioteke, Beijing). RNA solution was then transcribed to cDNA using Prime Script® RT reagent Kit With gDNA Eraser Kit (RR047A, Takara, Japan), and qRT-PCR was performed by automatic thermocycler (QuantStudio™ 6 Flex PCR, Life Technologies, MD, USA), with TB Green® Premix Ex Taq™ Kit (RR420A, Takara, Japan). The primers used in the process were listed (Supplementary Table 2).

Genomic DNA was extracted from *F. nucleatum* ATCC25586 using a bacterial DNA kit. A 183-bp fragment of *F. nucleatum* 16S rDNA was amplified via PCR with specific primers (F:5'-GGCCACAAGGGGAC TGAGACA-3'; R:5'-TTTAGCCGTCACTTCTTCTGTTGG-3'), purified, and quantified by NanoDrop. Copy numbers were calculated as: DNA (copies/μL) = [DNA concentration (ng/μL) × 6.022×10^{23}]/[product length (bp) × 660 g/mol × 1×10^{9}]. Ten-fold serial dilutions (10^{7}–10^{1} copies/μL) generated standard curves for qPCR quantification. Experimental sample copy numbers were derived from Ct-log plots. All amplicons were verified by Sanger sequencing and BLAST alignment against the GenBank database.

Histopathological assessment, AB-PAS, IHC, and IF staining

Colons were fixed in 10% formalin for 24 h and then made into paraffin sections (section thickness: 5 μm) and then stained with H&E and AB-PAS. The histopathological assessment was evaluated from two aspects: Crypt score: 0 = crypt integrity, 1 = disappearance of the bottom 1/3 crypt, 2 = disappearance of the bottom 2/3 crypt, 3 = disappearance of all crypts with intact surface epithelium, 4 = disappearance of all crypts and surface epithelium.

These changes are quantified as a percentage of affected area:1 = 1–25%, 2 = 26–50%, 3 = 51–75%, 4 = 100%. The product of the two is the crypt score. Inflammation score: 0 = no significant inflammation, 1 = inflammation confined to the mucosa, 2 = inflammation infiltrating into the submucosa layer, 3 = transmural inflammatory infiltration. These changes are quantified as a percentage of the area affected:1 = 1–25%, 2 = 26–50%, 3 = 51–75%, 4 = 76–100%. The product of the two is the inflammation score. The intestinal histopathological score was the sum of the crypt score and the inflammation score.

Colon paraffin sections and cells underwent dewaxing, rehydration, and antigen retrieval and were then incubated with 3% hydrogen peroxide (H_2O_2) to inactivate endogenous peroxidase activity. blocked with 3% bovine serum albumin (BSA) for 1 h at RT, and incubated with primary antibodies and secondary antibodies, DAB (BL732A, Biosharp, China) was used as the final chromogen. For IF, cells were fixed in 2% paraformaldehyde for 10 min at room temperature, washed with PBS, permeabilized for 10 min with 0.5% Triton X-100, and blocked for 1 h. Alexa Fluor-conjugated secondary antibodies were incubated for 1 h at room temperature, and the cell nucleus was counterstained with DAPI. For the detection of ROS, the C11-BODIPY 581/591 fluorescent probe (GC40165, GlpBio, USA) was used. For the detection of Fe^{2+}, FeRhoNox-1 fluorescent probe (MX4558, MaoKangbio, China), images were acquired with a fluorescence microscope (DMi8, LEICA, Germany) for confocal imaging.

Transmission electron microscopy (TEM)

Colon tissue and cells were prefixed with a 3% glutaraldehyde, then post-fixed in 1% osmium tetroxide, dehydrated in a series of acetone, infiltrated with Epon 812 resin and embedded. The semithin sections were stained with methylene blue, and the ultrathin sections were cut with a diamond knife, and stained with uranyl acetate and lead citrate. Sections were examined with a JEM-1400-FLASH transmission electron microscope.

In situ hybridization (FISH double labeling) assay

Tissue sections were dewaxed, digested with proteinase K, pre-hybridized with probes, hybridized with probes, washed, DAPI re-stained nuclei, sealed, and photographed by microscopy. Probe Information: Probe name: FUS664 (Green), Probe sequence: CUUGUAGUUUCCGCUACCUC, Probe marker: 5'6-FAM, RNA, 3'6-FAM. Probe name: EUB338 (red), Probe sequence: GCUGCCUCCCGUAGGAGU, Probe marker: 5'CY3, RNA, 3'CY3. Quantification was normalized to EUB338 signals to account for spatial heterogeneity[23].

Determination of permeability

One day after the last periodontal inoculation with *F. nucleatum* (on Day 37), the mice were fasted on solids and liquids for 4 h and then were gavaged with FD4 (Sigma-Aldrich, USA) (60 mg/100 g body weight). Four hours later, they were euthanized, and blood was collected by cardiac puncture. The serum was obtained by centrifugation. The concentration of FD4 was detected using a fluorescence microplate reader (Thermo, USA) at 485 nm, excitation, and 525 nm, emission[51].

16S ribosomal RNA (16S rRNA) gene sequencing

Total microbial DNA was extracted according to the instructions of the E.Z.N.A.® soil DNA kit (Omega Bio-tek, Norcross, GA, USA), and the quality of the DNA extracted was checked by agarose gel electrophoresis with 1% agarose, and DNA concentration and purity were quantified using a NanoDrop2000 spectrophotometer (Thermo Fisher Scientific, USA). PCR amplification of the 16S rRNA gene V3–V4 hypervariable regions was performed using barcoded primers: Forward primer 338 F: 5'-ACTCCTACGGGAGGCAGCAG-3'; Reverse primer 806 R: 5'-GGACTACHVGGGTWTCTAAT-3'[53]. PCR products from the same samples were mixed and recovered on a 2% agarose gel, purified using the AxyPrep DNA Gel Extraction Kit (Axygen Biosciences, CA, USA), detected by electrophoresis on a 2% agarose gel, and quantified by quantitative assay using the Quantus™ Fluorometer (Promega, USA). Fluorometer (Promega, USA) for quantification of the recovered products. Library construction was performed using the NEXTflexTM Rapid DNA-Seq Kit (Bioo Scientific, USA). Sequencing using Illumina's Miseq PE300/NovaSeq PE250 platforms. The paired-end raw sequencing reads were first subjected to quality control using fastp[54] (version 0.19.6; https://github.com/OpenGene/fastp), followed by sequence merging with FLASH[55] (version 1.2.11; http://www.cbcb.umd.edu/software/flash). Chimeric sequences were removed, and operational taxonomic units (OTUs) were clustered at 97% similarity using UPARSE v7.1[56](http://drive5.com/uparse/). Taxonomic annotation of OTUs was performed via the RDP classifier[57] (version 2.11; http://rdp.cme.msu.edu/) against the 16S rRNA gene database with a confidence threshold of 70%, generating community composition profiles across taxonomic levels. Functional potential prediction was conducted using PICRUSt2 (version 2.2.0). All analyses were implemented on the Majorbio Cloud Platform (https://cloud.majorbio.com). Alpha diversity differences between groups were assessed via the Wilcoxon rank-sum test. Beta diversity was evaluated through principal coordinate analysis (PCoA) based on Bray-Curtis distances, with statistical significance of microbial community structural differences determined by PERMANOVA. LEfSe analysis[58](http://huttenhower.sph.harvard.edu/LEfSe) identified differentially abundant bacterial taxa at the family level (LDA score >2, $p < 0.05$).

Liquid chromatograph-mass spectrometer (LC-MS) analysis

The extraction of 50 mg intestinal content was settled at −20 °C and treated by high-throughput tissue crusher Wonbio-96c (Wanbo Biotechnology Co., LTD, China) at 50 Hz for 6 min, then followed by vortex for 30 s and ultrasound at 40 kHz for 30 min at 5 °C. The samples were placed at −20 °C for 30 min to precipitate proteins. After centrifugation at 13,000 × *g* at 4 °C for 15 min, the supernatant was transferred to sample vials for LC-MS/MS analysis. Chromatographic separation of the metabolites was performed on a Thermo UHPLC system equipped with an ACQUITY BEH C18 column (100 mm × 2.1 mm i.d., 1.7 μm; Waters, Milford, USA). After UPLC-TOF/MS analyses, the raw data were imported into the Progenesis QI 2.3 (Nonlinear Dynamics, Waters, USA) for peak detection and alignment. Differential metabolites were annotated to metabolic pathways using the KEGG PATHWAY database (https://www.kegg.jp/kegg/pathway.html). Pathway enrichment analysis was performed with the Python scipy.stats package, and Fisher's exact test was applied to identify the biological pathways most significantly associated with experimental treatments[59].

Statistical analysis

Statistical data were analyzed by SPSS version 21.0 (IBM, Chicago, IL). Data were represented as mean ± SEM. Experimental data and graphs were prepared by GraphPad Prism 9.0 software (La Jolla, CA, USA). Differences among groups were analyzed using one-way or two-way ANOVA with Tukey's multiple comparisons test, followed by a post hoc test if data were normally distributed. Otherwise, Kruskal–Wallis and Mann–Whitney *U* tests were used to evaluate differences. The significance of the Kaplan–Meier survival analysis was calculated by the Log-rank test. The rank-sum test was used for data with unequal variances. $p < 0.05$ was considered statistically significant.

Data availability

All data supporting the findings of this study are available within the paper and its Supplementary Information.

Received: 26 August 2024; Accepted: 20 June 2025;
Published online: 09 August 2025

References

1. Febbraio, M., Roy, C. B. & Levin, L. Is there a causal link between periodontitis and cardiovascular disease? A concise review of recent findings. *Int. Dent. J*. **72**, 37–51 (2022).
2. AlSharief, M. & Alabdurubalnabi, E. Periodontal pathogens and adverse pregnancy outcomes: a narrative review. *Life* **13**, 1559 (2023).
3. Wang, H. et al. Clonal hematopoiesis driven by mutated DNMT3A promotes inflammatory bone loss. *Cell* **187**, 3690–3711.e19 (2024).
4. Di Spirito, F. et al. The association between periodontitis and human colorectal cancer: Genetic and pathogenic linkage. *Life* **10**, 1–18 (2020).
5. Zhang, Y. et al. The association between periodontitis and inflammatory bowel disease: a systematic review and meta-analysis. *Biomed Res. Int*. https://doi.org/10.1155/2021/6692420 (2021).
6. Janakiram, C. & Dye, B. A. A public health approach for prevention of periodontal disease. *Periodontol 2000* **84**, 202–214 (2020).
7. Kwon, T., Lamster, I. B. & Levin, L. Current concepts in the management of periodontitis. *Int. Dent. J.* **71**, 462–476 (2021).
8. Wu, L., Zhang, S., Zhao, L., Ren, Z. & Hu, C. Global, regional, and national burden of periodontitis from 1990 to 2019: results from the Global Burden of Disease study 2019. *J. Periodontol.* **93**, 1445–1454 (2022).
9. Kobayashi, T. et al. Ulcerative colitis. *Nat. Rev. Dis. Prim.* **6**, 74 (2020).
10. Kucharzik, T., Koletzko, S., Kannengießer, K. & Dignaß, A. Ulcerative colitis—diagnostic and therapeutic algorithms. *Dtsch. Arztebl. Int.* https://doi.org/10.3238/arztebl.2020.0564 (2020).
11. Lorenzo-Pouso, A. I., Castelo-Baz, P., Rodriguez-Zorrilla, S., Pérez-Sayáns, M. & Vega, P. Association between periodontal disease and inflammatory bowel disease: a systematic review and meta-analysis. *Acta Odontol. Scand.* **79**, 344–353 (2021).
12. de Mello-Neto, J. M., Nunes, J. G. R., Tadakamadla, S. K. & Figueredo, C. M. da S. Immunological traits of patients with coexistent inflammatory bowel disease and periodontal disease: a systematic review. *Int. J. Environ. Res. Public Health* https://doi.org/10.3390/ijerph18178958 (2021).
13. Wang, Q., Chen, S., Zhou, J. & Zhao, L. Bidirectional associations between periodontitis and inflammatory bowel disease: a systematic review of longitudinal studies with meta-analysis and trial sequential analysis. *J Periodontal Res.* https://doi.org/10.1111/jre.13291 (2024).
14. Lin, C. Y. et al. Increased risk of ulcerative colitis in patients with periodontal disease: a nationwide population-based cohort study. *Int. J. Environ. Res. Public Health* **15**, 2602 (2018).
15. Habashneh, R. A., Khader, Y. S., Alhumouz, M. K., Jadallah, K. & Ajlouni, Y. The association between inflammatory bowel disease and periodontitis among Jordanians: a case–control study. *J. Periodontal Res.* **47**, 293–298 (2012).
16. Socransky, S. S., Haffajee, A. D., Cugini, M. A., Smith, C. & Kent Jr, R. L. LKent Jr, R. Microbial complexes in subgingival plaque. *J. Clin. Periodontol* **25**, 134–144 (1998).
17. Song, B. et al. *Akkermansia muciniphila* inhibited the periodontitis caused by Fusobacterium nucleatum. *NPJ Biofilms Microbiomes* **9**, 49 (2023).
18. Lin, S. et al. *Fusobacterium nucleatum* aggravates ulcerative colitis through promoting gut microbiota dysbiosis and dysmetabolism. *J. Periodontol.* **94**, 405–418 (2023).
19. Chaushu, S. et al. Direct recognition of *Fusobacterium nucleatum* by the NK cell natural cytotoxicity receptor NKp46 aggravates periodontal disease. *PLoS Pathog.* **8**, e1002601 (2012).
20. Ma, C., Luo, H., Gao, F., Tang, Q. & Chen, W. *Fusobacterium nucleatum* promotes the progression of colorectal cancer by interacting with E-cadherin. *Oncol. Lett.* **16**, 2606–2612 (2018).
21. Strauss, J. et al. Invasive potential of gut mucosa-derived *Fusobacterium nucleatum* positively correlates with IBD status of the host. *Inflamm. Bowel Dis.* **17**, 1971–1978 (2011).
22. Swidsinski, A. et al. Acute appendicitis is characterised by local invasion with *Fusobacterium nucleatum/necrophorum*. *Gut* **60**, 34–40 (2011).
23. Chen, Y. et al. *Fusobacterium nucleatum* facilitates ulcerative colitis through activating IL-17F signaling to NF-κB via the upregulation of CARD3 expression. *J. Pathol.* **250**, 170–182 (2020).
24. Liu, L. et al. *Fusobacterium nucleatum* aggravates the progression of colitis by regulating M1 macrophage polarization via AKT2 pathway. *Front. Immunol.* **10**, 1324 (2019).
25. Turner, J. R. Intestinal mucosal barrier function in health and disease. *Nat. Rev. Immunol*. **9**, 799–809 (2009).
26. Subramanian, S., Geng, H. & Tan, X.-D. Cell death of intestinal epithelial cells in intestinal diseases. *Acta Physiol. Sin.* **72**, 308–324 (2020).
27. Dixon, S. J. et al. Ferroptosis: an iron-dependent form of nonapoptotic cell death. *Cell* **149**, 1060–1072 (2012).
28. Ursini, F. & Maiorino, M. Lipid peroxidation and ferroptosis: the role of GSH and GPx4. *Free Radic. Biol. Medic.* **152**, 175–185 (2020).
29. Doll, S. et al. ACSL4 dictates ferroptosis sensitivity by shaping cellular lipid composition. *Nat. Chem. Biol.* **13**, 91–98 (2017).
30. Xie, Y. et al. Ferroptosis: process and function. *Cell Death Differ.* **23**, 369–379 (2016).
31. Kobayashi, Y. et al. Association between dietary iron and zinc intake and development of ulcerative colitis: a case–control study in Japan. *J. Gastroenterol. Hepatol.* **34**, 1703–1710 (2019).
32. Chen, Y., Zhang, P., Chen, W. & Chen, G. Ferroptosis mediated DSS-induced ulcerative colitis associated with Nrf2/HO-1 signaling pathway. *Immunol. Lett.* **225**, 9–15 (2020).
33. Xu, M. et al. Ferroptosis involves in intestinal epithelial cell death in ulcerative colitis. *Cell Death Dis.* **11**, 86 (2020).
34. Brennan, C. A. & Garrett, W. S. Fusobacterium nucleatum — symbiont, opportunist and oncobacterium. *Nat. Rev. Microbiol*. **17**, 156–166 (2019).

35. Baima, G. et al. Shared microbiological and immunological patterns in periodontitis and IBD: a scoping review. *Oral Dis*. **28**, 1029–1041 (2022).
36. Dzink, J. L., Sheenan, M. T. & Socransky, S. S. Proposal of three subspecies of *Fusobacterium nucleatum* Knorr 1922: *Fusobacterium nucleatum* subsp. *nucleatum* subsp. nov., comb. nov.; *Fusobacterium nucleatum* subsp. *polymorphum* subsp. nov., nom. rev., comb. nov.; and *Fusobacterium nucleatum* subsp. *vincentii* subsp. nov., nom. rev., comb. nov. *Int. J. Syst. Bacteriol.* **40**, 74–78 (1990).
37. Thurnheer, T., Karygianni, L., Flury, M. & Belibasakis, G. N. *Fusobacterium* species and subspecies differentially affect the composition and architecture of supra- and subgingival biofilms models. *Front. Microbiol.* **10**, 1716 (2019).
38. Qu, H. et al. A rapid and sensitive CRISPR-Cas12a for the detection of *Fusobacterium nucleatum*. *Microbiol. Spectr.* **12**, e0362923 (2024).
39. Ternes, D. et al. The gut microbial metabolite formate exacerbates colorectal cancer progression. *Nat. Metab.* **4**, 458–475 (2022).
40. Thursby, E. & Juge, N. Introduction to the human gut microbiota. *Biochem. J*. **474**, 1823–1836 (2017).
41. Cai, Z., Zhu, T., Liu, F., Zhuang, Z. & Zhao, L. Co-pathogens in periodontitis and inflammatory bowel disease. *Front. Med.* https://doi.org/10.3389/fmed.2021.723719 (2021).
42. Gheorghe, D. N. et al. Periodontitis, metabolic and gastrointestinal tract diseases: current perspectives on possible pathogenic connections. *J. Pers. Med.* https://doi.org/10.3390/jpm12030341 (2022).
43. Xun, Z., Zhang, Q., Xu, T., Chen, N. & Chen, F. Dysbiosis and ecotypes of the salivary microbiome associated with inflammatory bowel diseases and the assistance in diagnosis of diseases using oral bacterial profiles. *Front. Microbiol.* **9**, 1136 (2018).
44. Bao, J. et al. Periodontitis may induce gut microbiota dysbiosis via salivary microbiota. *Int. J. Oral Sci.* **14**, 32 (2022).
45. Qian, J. et al. Periodontitis salivary microbiota worsens colitis. *J. Dent. Res.* **101**, 559–568 (2022).
46. Li, L. et al. Gut microbiota may mediate the influence of periodontitis on prediabetes. *J. Dent. Res.* **100**, 1387–1396 (2021).
47. Kitamoto, S. & Kamada, N. Periodontal connection with intestinal inflammation: microbiological and immunological mechanisms. *Periodontology 2000* https://doi.org/10.1111/prd.12424 (2022).
48. Kitamoto, S. et al. The intermucosal connection between the mouth and gut in commensal pathobiont-driven colitis. *Cell* **182**, 447–462.e14 (2020).
49. Jin, J., Liu, X. & Shiroguchi, K. Long journey of 16S rRNA-amplicon sequencing toward cell-based functional bacterial microbiota characterization. *iMetaOmics* **1**, e9 (2024).
50. Su, W. et al. *Fusobacterium nucleatum* promotes the development of ulcerative colitis by inducing the autophagic cell death of intestinal epithelial. *Front. Cell Infect. Microbiol.* **10**, 594806 (2020).
51. Liu, L., Liang, L., Yang, C., Zhou, Y. & Chen, Y. Extracellular vesicles of *Fusobacterium nucleatum* compromise intestinal barrier through targeting RIPK1-mediated cell death pathway. *Gut Microbes* **13**, 1–20 (2021).
52. Xu, T. et al. Dextran sulfate sodium-induced colitis exacerbates periodontitis via the NADPH oxidase 2/reactive oxygen species axis in M1-like macrophages. *hLife* https://doi.org/10.1016/j.hlife.2025.01.006 (2025).
53. Liu, C. et al. Denitrifying sulfide removal process on high-salinity wastewaters in the presence of *Halomonas* sp. *Appl. Microbiol. Biotechnol.* **100**, 1421–1426 (2016).
54. Chen, S., Zhou, Y., Chen, Y. & Gu, J. fastp: an ultra-fast all-in-one FASTQ preprocessor. *Bioinformatics* **34**, i884–i890 (2018).
55. Magoč, T. & Salzberg, S. L. FLASH: fast length adjustment of short reads to improve genome assemblies. *Bioinformatics* **27**, 2957–2963 (2011).
56. Edgar, R. C. UPARSE: highly accurate OTU sequences from microbial amplicon reads. *Nat. Methods* **10**, 996–998 (2013).
57. Stackebrandt, E. & Goebel, B. M. Taxonomic note: a place for DNA-DNA reassociation and 16S rRNA sequence analysis in the present species definition in bacteriology. *Int. J. Syst. Evol. Microbiol.* **44**, 846–849 (1994).
58. Segata, N. et al. Metagenomic biomarker discovery and explanation. *Genome Biol.* **12**, R60 (2011).
59. Ren, Y. et al. Majorbio cloud: a one-stop, comprehensive bioinformatic platform for multiomics analyses. *iMeta* **1**, e12 (2022).

Acknowledgements

This work was supported by the National Natural Science Foundation of China (grant # 81970944), the National Natural Science Foundation of China Youth Program (grant # 82301089), Develop Program, the Natural Science Foundation of Sichuan Province (grant # 2023NSFSC0553), West China Hospital of Stomatology Sichuan University (grant # RCDWJS2024-(2)), and Research and Develop Program, West China Hospital of Stomatology Sichuan University (RD-03-202105). And we thank Majorbio® for providing the 16S rRNA gene sequencing and LC-MS platform.

Author contributions

L.Z. and L.C. contributed to the conception and design and critically revised the manuscript; X.Z. contributed to the conception and design, acquisition, analysis, and interpretation, drafted the manuscript, and critically revised the manuscript; S.S. and Q.W. contributed to the acquisition, analysis, and interpretation; J.Z. and H.W. contributed to the conception and design and critically revised the manuscript. All authors gave final approval and agreed to be accountable for all aspects of the work.

Competing interests

The authors declare no competing interests.

Additional information

Supplementary information The online version contains supplementary material available at https://doi.org/10.1038/s41522-025-00763-1.

Correspondence and requests for materials should be addressed to Lei Cheng or Lei Zhao.